

Article

Microstructure and Properties of the Interface Area in the Laser Cladded Ni Based Coatings on the 1Cr10Mo1NiWVNbN Steel

Yunxia Chen *, Yanbing Guo, Binfeng Lu, Mengjia Xu and Jianhui Xu

School of Mechanical Engineering, Shanghai Dianji University, Shanghai 201306, China; yanbingg1984@126.com (Y.G.); lubf@sdju.edu.cn (B.L.); xumj@sdju.edu.cn (M.X.); xujh@sdju.edu.cn (J.X.)

* Correspondence: cyx1978@yeah.net; Tel.: +86-21-3822-6089; Fax: +86-21-3822-3186

Academic Editor: Håkan Hallberg

Received: 21 January 2017; Accepted: 10 May 2017; Published: 15 May 2017

Abstract: The Ni-based coatings were deposited on the 1Cr10Mo1NiWVNbN steel by using laser cladding process. The microstructure and properties of the coatings interface area were investigated by OM (Optical Microscopy), SEM (Scanning Electron Microscope), XRD (X-Ray Diffraction) microhardness test and EDS (Energy Spectrum Analysis) analysis. The results show that the bonding condition of the coatings interface is different in the monolayer and the trilayer. The monolayer coatings have a small dilution area. The dilution rate in a coating layer increases by layers. The scale of ferrite (α) phase increases with the layer increases. The surface cladding quality of a monolayer is better than that of the trilayer coatings. The width of the interface increases with the increase of the layer. The width of the interface region in the trilayer coatings increases significantly. The microhardness of the interface zone is much higher than that in the coatings zone and the substrate zone. The microhardness of trilayer coatings is higher than that of the monolayer.

Keywords: coatings; laser cladding; Ni-based powder; microstructure; properties

1. Introduction

Currently, the environmental and financial constraints on power generation plant have focused on higher efficiency and lower emission systems. The thermal efficiency of the power plant is most effectively achieved by increasing the temperature and, to a lesser extent, the pressure of the steam entering the turbine. The ferrite stainless steel of 12% chromium content is a determinant steel in the ultra-supercritical power generation units in the nuclear power plant [1,2]. Depending on their better corrosion resistance and lower cost compared to austenitic stainless steels, both the use and welding of low and medium grades of ferrite stainless steels have received considerable interests for power industry applications [3–6]. 1Cr10Mo1NiWVNbN is among those steels which have high strength creep resistance used as turbine blade and rotors in the nuclear power plant [7–9]. Therefore, the welding is an indispensable process for the manufacturing and repairing of the power plant products with 1Cr10Mo1NiWVNbN [10].

Ni-based alloy is widely used as welding and repairing materials [11,12] for its good weldability, thermal mechanical properties and creep resistance. However, it is not suitable for application in the welding process of high-precision parts and complex structures due to its high residual welding stress and bulk welding deformation. To deal with this problem, low heat input and small distortion cladding process is usually an optimized option in repairing high chromium steel parts with Ni-based alloys [13,14]. The interface of dissimilar materials is the critical area in 1Cr10Mo1NiWVNbN steel part of Ni-based coatings. Microstructure and properties in both sides are determinant for the reliability of power plant products [15]. However, details of microstructural evolution of dissimilar

bonding interface in ferritic stainless steel and Ni-based alloys have not been fully understood. For instance, the cladding parameters will affect the evolution of microstructure and micro-hardness of the coatings [16].

In this paper, Ni-based alloy coatings were fabricated on the 1Cr10Mo1NiWVNbN substrate by laser cladding. The microstructure, distribution of elements, and hardness of the laser cladded coatings were investigated to characterized to obtain the microstructures and properties of the laser cladded Ni-based coatings in 1Cr10Mo1NiWVNbN steel. The main objective of this study is to reveal the microstructure and mechanical properties of the Ni-based coatings deposited on the high chromium steel by laser cladding.

2. Materials and Experimental Procedures

Laser cladded Ni-based coatings were fabricated by DL-LPM-III CO₂ laser system equipped with an argon shielding gas device. Ni-based spherical particles powder with size of 75–250 μm were chosen as the deposition materials. 1Cr10Mo1NiWVNbN steel plate was chosen as the substrate with dimensions of 150 mm × 15 mm × 12 mm. The morphology of the Ni-based powder is shown in Figure 1. The chemical composition of the powder and the substrate were tested by EPMA (Electron probe micro-analyzer, Vario EL Cube, Elementar Trading Shanghai, Shanghai, China), as listed in Table 1.

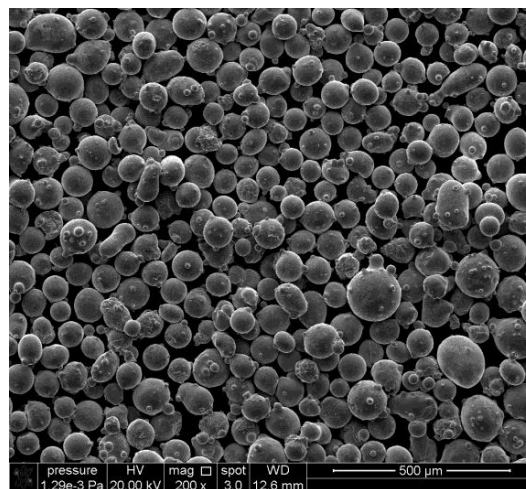


Figure 1. Morphology of the Ni-based alloy powder for laser cladding.

Table 1. Chemical composition of the powder and substrate (wt %).

Materials	Element												
	C	Si	Cr	B	Fe	Ni	Mn	Mo	Nb	W	V	P	S
Powder	0.80	3.5	16	3.6	4.2	Bal.	-	-	-	-	-	-	-
Substrate	0.14	0.22	11	-	Bal.	-	0.58	1.2	0.05	0.3	0.2	0.02	0.02

The substrate surface was polished and cleaned with acetone and alcohol before laser cladding to eliminate stains or contaminants. The wavelength of the laser beam was 1064 nm, and the circular spot size of the laser at the focal length (165 mm) was 4 mm (diameter). The optimized laser processes parameters and deposited layer parameters are listed in Table 2. High-purity argon gas was invoked as shielding gas through the copper nozzle with a flow rate of 5 L/min to prevent the melted pool from oxidation during the cladding process. The specimens were quenched in water after the laser cladding process. The quenched specimens were sectioned across the cross-sectional plane, then polished and etched by using 4% nitalacid solutions (4% nitric acid and 96% ethanol).

The microstructure and morphology of the coatings were characterized using a NIKON EPIPHOT 300 optical microscopy (OM, Nikon Metrology, Tokyo, Japan) and field emission scanning electron microscopy (FE-SEM HITACHI S-3400N, Hitachi, Tokyo, Japan) equipped with Inca Energy energy-dispersive spectrometer (EDS, Oxford Instruments, Oxford, UK). X-ray experiments were conducted using a Ultima IV X-ray diffractometer (Rigaku Corporation, Tokyo, Japan) and a scanning rate of 1° min^{-1} over the range $2\theta = 20^\circ\text{--}110^\circ$, with unfiltered Cu K α radiation. The system was operated at 40 kV and 30 mA.

The microhardness along the cross profile of the coatings was measured by a Vickers microhardness tester (Zwick/Roell ZH μ , Zwick Roell, Ulm, Germany) with a 1 kg load and 15 s loading time.

Table 2. Processing parameters for laser cladding and cladding layers.

Scheme	Laser Power (kW)	Scanning Velocity (mm/s)	Spot Diameter (mm)	Layers Number
1	3.6	7	4	1
2	3.6	7	4	3

3. Results and Discussion

3.1. Solidification Microstructure

The section morphologies of monolayer and trilayer coatings are shown in Figure 2. There is no pores or cracks observed in the coatings. The thickness of monolayer coatings is about 1.0 mm, while the thickness of trilayer coatings is 2.4 mm. The coatings consist of the coating, the heat affect zone and the substrate, respectively, as shown in Figure 2. The color contrast of the etched microstructure indicates that Ni-based coatings has a higher brightness than that of Fe-based substrate. The possible reason is that Ni-based microstructure has better corrosion resistance than that of high chromium steel. The thickness and width of trilayer coatings are higher than that of monolayer coatings. This phenomenon can be attributed to much more total heat input, powder presetting of the prior layer, surface tension, and flow of the molten pool during the trilayer cladding process [17].

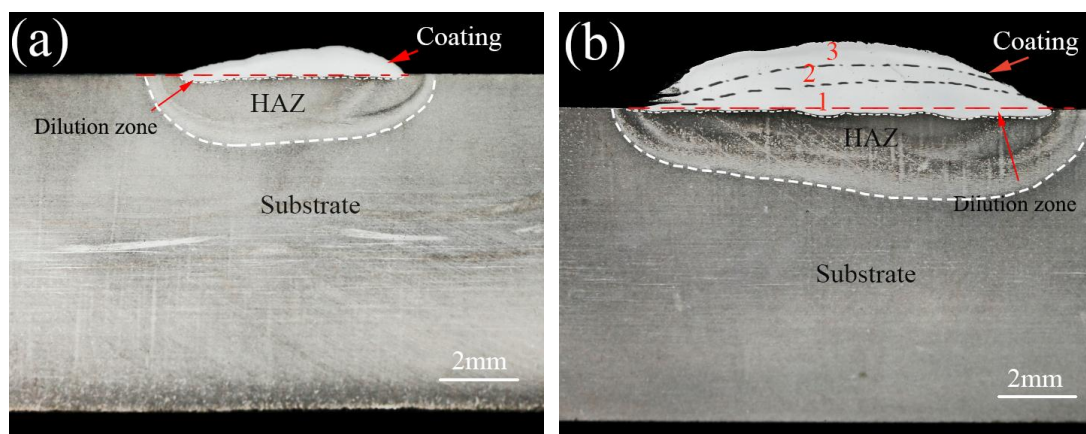


Figure 2. The profiles of cladded coatings with different layers (a) monolayer and (b) trilayer.

The dilution zone of the coatings is defined as the area between the planar growth layer (including the planar growth layer) and the original surface of the substrate (as shown in Figure 2). The depths of dilution zone of monolayer and trilayer coatings are similar, which indicates that the laser cladding process of the second and the third layer's heat input cannot melt the interface area of first layer. The samples of trilayer coatings should be cooled to ambient temperature before the next layer cladding process, to ensure low dilution of the coatings (usually this rate should be minus 5%).

The dilution rate (η) of the clad coatings with different layers is calculated by using the equation of $\eta = \frac{S_2}{S_1 + S_2}$, where S_2 is the dilution zone of the coatings as can be seen in Figure 2, S_1 is the area of the coatings above the original surface line of the substrate. The calculated dilution rates of the coatings are listed in Table 3. The dilution zone area of monolayer and trilayer coatings is similar, but compared to monolayer coatings, trilayer coatings have more total surface area. Therefore, the dilution rate of monolayer coatings is higher than that of trilayer coatings.

Table 3. The dilution rate of monolayer and trilayer coatings.

Laser Power (kW)	Number of Layers	Thickness (mm)	Width (mm)	Dilution Rate (%)
3.6	1	0.9	5.7	7.8
3.6	3	2.6	8.3	3.3

3.2. The Microstructure in the Coatings

Laser cladding is a rapid solidification process that will cause the fine dendrite to grow. Figure 3 shows dendrite morphology and microstructure at the interface area of the coatings obtained after monolayer and trilayers cladding process. As shown in Figure 3a, the columnar dendrite clusters averagely distribute in the center area of the coatings. Fine scale dendrites indicate that the cooling rate is high during the solidification process. Finer equiaxed grain distributed at the top surface of the coatings indicates that the cooling rate is higher than that of the center of coatings. The details of the interface area between the coating and substrate of the monolayer and trilayer coatings are shown in Figure 3b,c, respectively.

In this study, the dendritic microstructures of different phases in coatings are revealed through the differences in etching tendency of interdendritic regions and inner dendritic area that refer to the difference of composition [18].

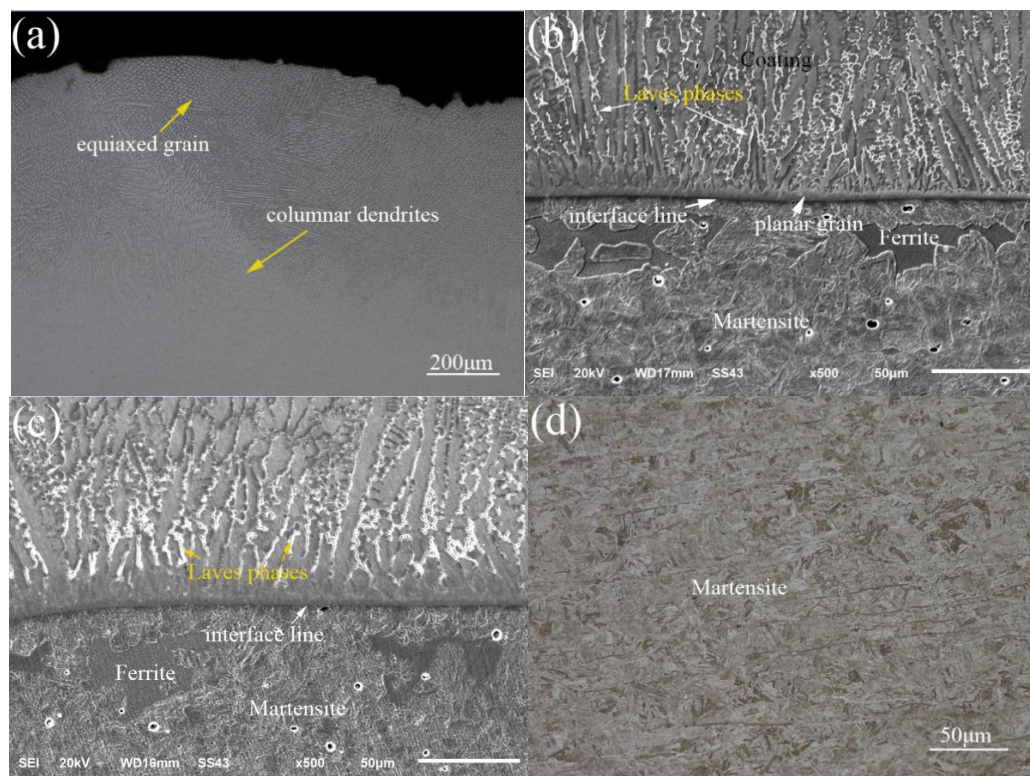


Figure 3. The dendritic morphology (a) and SEM microstructures at interface area of the substrate and coating material of monolayer (b) and trilayer (c) coatings, (d) microstructure of the substrate.

The secondary arms with dark line shapes and primary arms with island or long chain shapes can be observed at the interdendritic regions. The interior areas of islands or chains have lower insensitization corrosion tendency than that of the boundaries. The laves phase distributes in the interdendritic area with bright color, as shown in Figure 3b,c. Because of the relatively higher corrosion resistance at the grain boundaries [16], these regions are difficult to etch to present white lines. The phase distributed in the inner area of the dendrite is the γ phase, the different phases of the inner and interdendritic regions are caused by chemical segregation during the solidification process.

The scale of laves phase distributed in trilayer coatings is larger than that in the monolayer. The heat input of the second and third layer in the laser cladding process always affects the initial microstructure of the prior coatings, meanwhile, the heat input is a driving force for laves phase growth. Thin planar grains are distributed above the interface line and below the dendrite area as a result of the high cooling rate at this area. An obvious interface line can be observed below the planar grains. The microstructure below the interface line is fine lath martensite and acicular ferrite distributed inside of the martensite lathes. Some blocky ferrite distributed near the interface line grew from the acicular ferrite, and the growth is caused by the heat effect from laser cladding process (as shown in Figure 4). Some pores are observed in the HAZ. It existed before the cladding process.

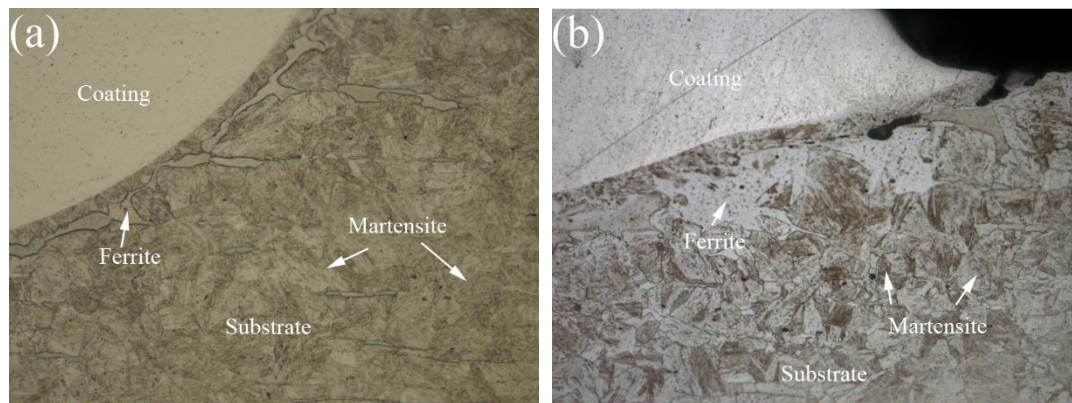


Figure 4. (a) OM microstructure of the monolayer and (b) trilayer coatings.

3.3. XRD Analysis

The X-ray diffraction results of laser cladding coatings are shown in Figure 5. The results show that the main phases of coatings are composed of γ -(Ni, Cr, Fe) solid solution, $\text{Fe}_3\text{Ni}_3\text{B}$, $\text{B}(\text{Fe}, \text{Si})_3$, CrB and laves phase. The characteristic peaks of the two patterns have slightly differences. Laves phase is always segregated at the interdendritic regions as a complex topological structure of AB_2 . It can be reasonably deduced that the regions with light color in interdendritic regions are laves phases combined with the relevant XRD patterns [19].

The fractions of each phase in the coatings can be indicated by the intensity of their characteristic peaks. The trilayer coatings have stronger intensity of CrB and laves phase. Therefore, the laves phase at the interface region of coatings increases with the increase of layer number.

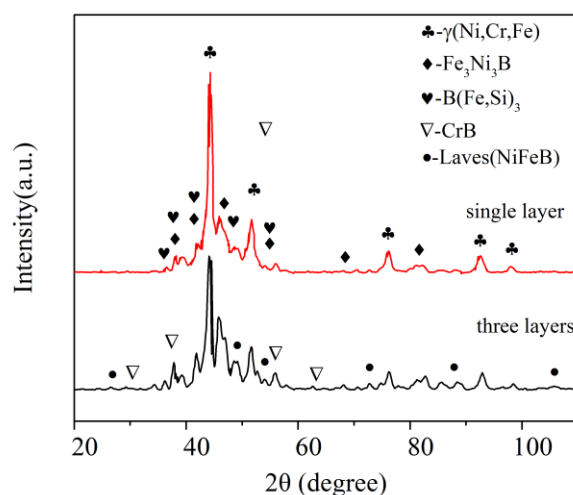


Figure 5. XRD patterns of the laser cladded monolayer and trilayers Ni-based coatings.

3.4. The Chemical Composition Distribution

The segregation of solute atoms in interdendritic regions of cladded coatings deviated markedly from the Brody–Flemings and Scheil equations, as a result of the large solute build-up at the dendrite tip under such a rapid solidification process [18]. Therefore, the solute concentration in the dendrite trunk is much higher than the equilibrium solidification in the laser cladded dendritic structure. Interdendritic chemical segregation in laser cladded coatings can be modified, but cannot be eliminated by laser cladding process. The solute distribution at one dimension was analyzed to clarify the segregation condition of the diluted area of the interface area in cladded coatings.

The X-ray energy dispersive spectroscopy line scans across the interface regions and the interior of the coatings are shown in Figure 6. The results show that all chemical compositions have an obvious fluctuation across the interface line. A slight intensity fluctuations can be observed on EDS line scan across the coatings area for C, Si, W, Mo, V, and Ni. It is indicated that these chemical compositions segregate at interdendritic regions. The segregations were initiated by a large difference in free energy between the stable solid and metastable liquid, which generally occurred lower than the liquids temperature during the rapid solidification of the laser cladding process [20]. Therefore, the assumption of a homogenous liquid was valid at the end of the solidification, and then the solutes segregated at interdendritic regions [18]. The concentration gradients of segregated elements across the interdendritic regions were caused by the formation of laves phases.

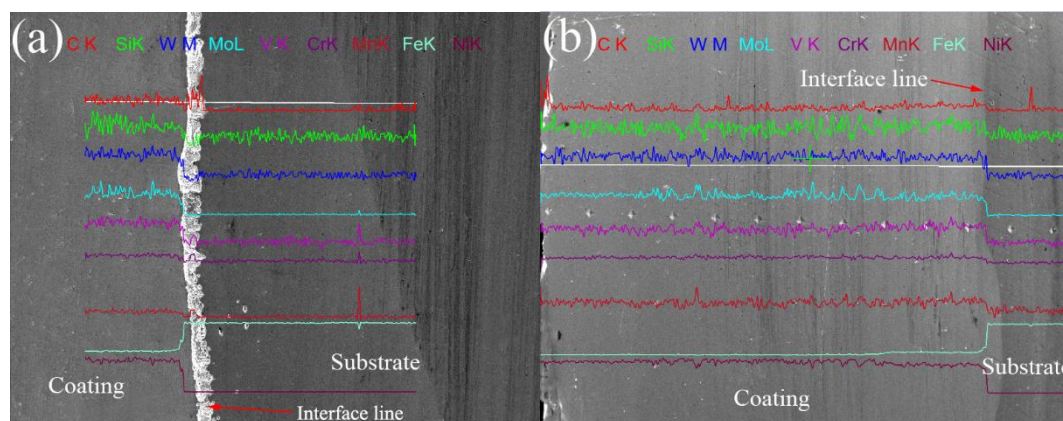


Figure 6. X-ray energy dispersive spectroscopy line scan across the interface region of the monolayer region (a) and trilayer coatings (b).

3.5. Microhardness

The segregation of solute atoms in interdendritic regions of clad coatings deviated markedly from the Brody–Flemings and Scheil equations, as a result of the large solute build-up at the dendrite tip under such a rapid solidification process [18]. Therefore, the solutes concentration in the dendrite trunk are much higher than the equilibrium solidification in the laser clad dendritic structure. Interdendritic chemical segregation in laser clad coatings can be modified, but cannot be eliminated by laser cladding process. The solute distribution at one dimension was analyzed to clarify the segregation condition of the diluted area of the interface area in clad coatings.

The X-ray energy dispersive spectroscopy line scans across the interface regions and the interior of the coatings are shown in Figure 6. The results show that all chemical compositions have an obvious fluctuation across the interface line. A slight intensity fluctuations can be observed on EDS line scan across the coatings area for C, Si, W, Mo, V, Ni. It is indicated that these chemical compositions segregate at interdendritic regions. The segregations were initiated by a large difference in free energy between the stable solid and metastable liquid, which were general occurred lower than the liquids temperature during the rapid solidification of the laser cladding process [20]. Therefore, the assumption of a homogenous liquid was valid at the end of the solidification, and then the solutes segregated at interdendritic regions [18]. The concentration gradients of segregated elements across the interdendritic regions were caused by the formation of laves phases.

The distributions of microhardness from the coating surface to the substrate are shown in Figure 7. The measurements of the Vickers hardness for laser clad coatings were taken in the cross-section perpendicular to the clad direction [21,22]. Before any series of tests, a calibration test was performed on a test piece of a known material's parameter on a daily basis to ensure that the results were within the normal range of reproducibility. For all hardness measurements, approximately five diagonals were measured at each load to yield a mean diagonal and standard deviation from which the hardness was calculated. Under an optical microscope, each indentation was measured diagonally from edge of the diamond shaped impression to the other edge, across each diagonal. The data were averaged to provide a mean diagonal length for each materials, the Vikers hardness value associated with each material was calculated using the relationship as the standard of ASTM E384-11:

$$H_V = 1.8544 \left(\frac{P}{d_V^2} \right)$$

where H_V was the diamond pyramid hardness in kg/mm^2 , P the applied load in kg, d_V the mean diagonal length in mm.

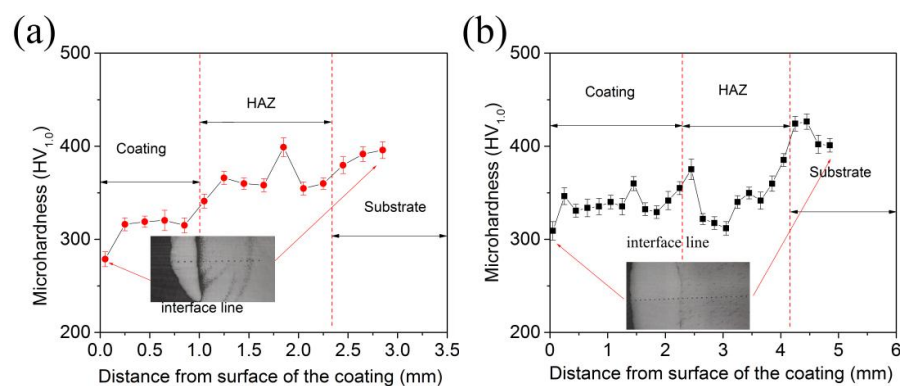


Figure 7. Microhardness of specimens as a function of distance from surface of monolayer (a) and trilayer coatings (b).

The results show that the average hardness of Ni-based coatings is lower than that of Fe-based substrate. This is due to the maintained phase of the substrate microstructure (martensite) with a high

dislocation density. High dislocation density and phase transformation process can result in high strain resistance microstructures [23,24]. The maintained microstructure of coatings is γ phase with face centered cubic structure. Compared with body centered cubic structure of Fe-based substrate, the γ phase has a relatively lower strain resistance. At the beginning the microhardness decreases, but increases from coating surface to substrate soon afterwards in trilayer coatings. The average hardness of the trilayer coatings is 337 HV. The hardness of HAZ near the interface line is lower than that of coatings, as shown in Figure 7a. The microhardness of the substrate is above 400 HV. The microhardness decreasing of the HAZ results from the precipitation and growth of blocky ferrites during three cladding process.

For the monolayer coating, the microhardness increases from the coatings surface to the substrate. The average microhardness of the monolayer coatings is 310 HV. The hardness of the HAZ is about 363 HV. It is higher than that of the coatings. This is because that the HAZ of the monolayer coatings only goes through one-time heat treatment process of laser cladding process. The scale of ferrite is smaller than that of the trilayer coatings as mentioned in Section 3.2. The average microhardness of the monolayer coatings is lower than that of the trilayer coatings. The reason for this phenomenon is that harder laves phase predicates in the prior layer coatings during multi-heat effect of the following layer cladding process in the trilayer coatings [25].

4. Conclusions

The Ni-based coatings were fabricated on the Fe-based high chromium content steel substrate by using CO₂ laser system. An optimized parameter (laser power of 3.6 kW, scanning speed of 7 mm/s) was used during monolayer and trilayer cladding processes. There were no pores or cracks observed in the coatings. The results show that the Ni-based powder is an ideal material to repair the 1Cr10Mo1NiWVNbN products that are used in steam turbines for ultra-supercritical unit in a nuclear power plant. The trilayer coating has good metallurgical bonding with substrate, and its dilution rate is constrained at a low value. The coatings is composed of thin planar grain at the bottom of the molten pool, columnar dendrite and fine equiaxed grain near the surface of the coating. The X-ray diffractometer results of the monolayer and the trilayer coatings both show that the main phase is γ (Ni, Cr, Fe), others are Fe₃Ni₃B, B(Fe, Si)₃, CrB, and laves (with AB₂ structure) characteristic peaks. The laves phase with bright color is observed at the interdendritic area at the center region of the coatings. The laves phase in the trilayer coatings grows to a greater scale owing to the heat treatment following a bilayer cladding process. The microhardness of the monolayer coatings increases from the surface to the substrate. The microhardness of the trilayer coatings firstly decreases, and then increases as a result of the increase of the blocky ferrite fraction in the trilayer coating. However, the average hardness of the monolayer coatings is lower than that of the trilayer coatings. This is because the scale of the laves phase increases in the trilayer coatings.

Acknowledgments: The authors gratefully acknowledge the financial support of the National Natural Science Foundation of China (Grant No. 51404125 and U1660101) and special foundation of Shanghai economic and Information Commission, No. JJ-YJCX-01-15-5718.

Author Contributions: Yunxia Chen and Yanbing Guo conceived and designed the experiments, analyzed the data and wrote the paper; Mengjia Xu and Bin Feng Lu performed the experiments; Jianhui Xu contributed analysis tools.

Conflicts of Interest: The authors declare no conflict of interest.

References

1. Shen, Y.; Shang, Z.; Xu, Z.; Liu, W.; Huang, X.; Liu, H. The nature of nano-sized precipitates in ferritic/martensitic steel P92 produced by thermomechanical treatment. *Mater. Charact.* **2016**, *119*, 13–23. [[CrossRef](#)]
2. Lu, F.; Liu, P.; Ji, H.; Ding, Y.; Xu, X.; Gao, Y. Dramatically enhanced impact toughness in welded 10% Cr rotor steel by high temperature post-weld heat treatment. *Mater. Charact.* **2014**, *92*, 149–158. [[CrossRef](#)]

3. Caballero, F.G.; Allain, S.; Cornide, J.; Puerta Velásquez, J.D.; Garcia-Mateo, C.; Miller, M.K. Design of cold rolled and continuous annealed carbide-free bainitic steels for automotive application. *Mater. Des.* **2013**, *49*, 667–680. [[CrossRef](#)]
4. Mani, A.A.; Kumar, T.S.; Chandrasekar, M. Mechanical and metallurgical properties of dissimilar welded components (AISI 430 ferritic–AISI 304 austenitic stainless steels) by CO₂ laser beam welding (LBW). *J. Chem. Pharm. Sci.* **2015**, *974*, 2115.
5. Bettahar, K.; Bouabdallah, M.; Badji, R.; Gaceb, M.; Kahloun, C.; Bacroix, B. Microstructure and mechanical behavior in dissimilar 13Cr/2205 stainless steel welded pipes. *Mater. Des.* **2015**, *85*, 221–229. [[CrossRef](#)]
6. Mourad, A.H.I.; Khourshid, A.; Sharef, T. Gas tungsten arc and laser beam welding processes effects on duplex stainless steel 2205 properties. *Mater. Sci. Eng. A* **2012**, *549*, 105–113. [[CrossRef](#)]
7. Yang, G.; Wang, L.; Ceng, S. Influences of Chemical Composition and Heat Treatment Process on Mechanical Properties of 1Cr10Mo1NiWVNbN Rotor Steel. *Mater. Mech. Eng.* **2009**, *8*, 17–21.
8. Ding, Z.; Hu, Q.; Zeng, L.; Li, J. Hot deformation characteristics of as-cast high-Cr ultra-super-critical rotor steel with columnar grains. *Int. J. Miner. Metall. Mater.* **2016**, *23*, 1275–1285. [[CrossRef](#)]
9. Wang, L.; Tai, Q.; Yang, G. Effect of the Cooling Speed on the Impact Toughness and Microstructure of 0Cr11Ni2MoVNb Steel. *Mater. Mech. Eng.* **2006**, *30*, 31–33.
10. Taban, E.; Deleu, E.; Dhooze, A. Laser welding of modified 12% Cr stainless steel: Strength, fatigue, toughness, microstructure and corrosion properties. *Mater. Des.* **2009**, *30*, 1193–1200. [[CrossRef](#)]
11. Hope, A.T.; Lippold, J.C. Development and testing of a high-chromium, Ni-based filler metal resistant to ductility dip cracking and solidification cracking. *Weld. World* **2017**, *61*, 325–332. [[CrossRef](#)]
12. Abe, T.; Sasahara, H. Dissimilar metal deposition with a stainless steel and nickel-based alloy using wire and arc-based additive manufacturing. *Precis. Eng.* **2016**, *45*, 387–395. [[CrossRef](#)]
13. Xu, G.; Kutsuna, M.; Liu, Z. Characteristics of Ni-based coating layer formed by laser and plasma cladding processes. *Mater. Sci. Eng. A* **2006**, *417*, 63–72. [[CrossRef](#)]
14. Martinsen, K.; Hu, S.J.; Carlson, B.E. Joining of dissimilar materials. *CIRP Ann Manuf. Technol.* **2015**, *64*, 679–699. [[CrossRef](#)]
15. Zhao, X.; Dang, Y.; Yin, H.; Yuan, Y.; Lu, J.; Yang, Z.; Gu, Y. Evolution of the microstructure and microhardness of a new wrought Ni–Fe based superalloy during high temperature aging. *J. Alloy. Compd.* **2015**, *644*, 66–70. [[CrossRef](#)]
16. Sexton, L.; Lavin, S.; Byrne, G. Laser cladding of aerospace materials. *J. Mater. Process. Technol.* **2002**, *122*, 63–68. [[CrossRef](#)]
17. Wen, S.; Li, S.; Wei, Q.; Yan, C.; Zhang, S.; Shi, Y. Effect of molten pool boundaries on the mechanical properties of selective laser melting parts. *J. Mater. Process. Technol.* **2014**, *214*, 2660–2667.
18. Kurz, W.; Fisher, D. *Fundamentals of Solidification*; Higher Education Press: Beijing, China, 2010; pp. 71–92.
19. Ye, X.; Hua, X.; Wang, M.; Lou, S. Controlling hot cracking in Ni-based Inconel-718 superalloy cast sheets during tungsten inert gas welding. *J. Mater. Process. Technol.* **2015**, *222*, 381–390. [[CrossRef](#)]
20. Zhang, L.; Danilova, E.V.; Steinbach, I.; Medvedev, D.; Galenko, P.K. Diffuse-interface modeling of solute trapping in rapid solidification: Predictions of the hyperbolic phase-field model and parabolic model with finite interface dissipation. *Acta Mater.* **2013**, *61*, 4155–4168. [[CrossRef](#)]
21. Jendrzejewski, R.; Conde, A.; de Damborenea, J.; Sliwinski, G. Characterisation of the laser-clad stellite layers for protective coatings. *Mater. Des.* **2002**, *23*, 83–88. [[CrossRef](#)]
22. Korsunsky, A.M.; McGurk, M.R.; Bull, S.J.; Page, T.F. On the hardness of coated systems. *Surf. Coat Technol.* **1998**, *99*, 171–183. [[CrossRef](#)]
23. Maruyama, K.; Sawada, K.; Koike, J. Strengthening mechanisms of creep resistant tempered martensitic steel. *ISIJ Int.* **2001**, *41*, 641–653. [[CrossRef](#)]
24. Krauss, G. Martensite in steel: Strength and structure. *Mater. Sci. Eng. A* **1999**, *273*, 40–57. [[CrossRef](#)]
25. Ram, G.D.J.; Reddy, A.V.; Rao, K.P. Control of Laves phase in Inconel 718 GTA welds with current pulsing. *Sci. Technol. Weld. Join.* **2004**, *9*, 390–398.

